Sub-Wavelength Focusing at the Multi-Wavelength Range Using Superoscillations: An Experimental Demonstration

Alex M. H. Wong and George V. Eleftheriades, *Fellow, IEEE*

***Abstract*—We experimentally demonstrate the formation of a superoscillatory sub-wavelength focus at a multi-wavelength working distance. We first discuss and distinguish superlensing, superdirectivity and superoscillation as different methods which, in their respective ways, achieve sub-diffraction resolution. After establishing superoscillation as a potential way towards sub-wavelength focusing at the multi-wavelength range, we proceed to design, synthesize and demonstrate a superoscillatory sub-wavelength focus in a waveguide environment. Our measurements confirm the formation of a focus at 75% the spatial width of the diffraction limited sinc pulse, 4.8 wavelengths away from the source distributions. This working distance is an order of magnitude extended from those of superlenses and related evanescent-wave-based devices, and should pave way to various applications in high-resolution imaging.**

***Index Terms*—Diffraction limit, image resolution, sub-wavelength focusing, superdirectivity, superoscillation.**

I. Introduction

THE diffractive nature of electromagnetic waves has traditionally been viewed as a fundamental limit on the resolution of imaging systems, blurring image details at length scales smaller than half the imaging wavelength. Notwithstanding, there has been intensive interest towards developing imaging systems with resolution beyond the conventional limit of diffraction. An early example of imaging beyond the diffraction limit was Synge's proposal [1] which eventually became the near-field scanning optical microscope. More recently, Veselago and Pendry's proposal of a superlens [2], [3] triggered various clever ideas which used evanescent electromagnetic fields to image beyond the diffraction limit [4]–[11]. While these ideas extend the imaging device's working distance to about a quarter of the imaging wavelength, this distance remains constrained to the evanescent near-field of the imaging device. On a related front, the superdirective antenna, proposed by Schelkunoff in 1943 [12], could in principle squeeze an antenna main beam beyond that emanating from a uniform aperture of the same size. This constitutes the achievement of directivity beyond the angular diffraction limit. Nonetheless, as antenna pattern formation occurs in the far-field, the superdirective antenna does not really provide imaging capability beyond the spatial diffraction limit. We shall elaborate on these claims later in this paper.

The phenomenon of superoscillation holds promise to sub-diffraction imaging beyond the constraining extent of evanescent near-field. While the discovery of superoscillations [13], [14] and their linkage to spatial domain electromagnetic waves [15] predate Pendry's superlens proposal, superoscillatory wave-based imaging has not seen much research interest, perhaps due to the perception that required sensitivity levels and achievable power efficiencies would render most potential application impractical. Nonetheless, theoretical procedures have been proposed which design superoscillatory waveforms [15]–[17]; experimental observations of pseudorandom superoscillatory waveforms have also been reported [18], [19]. However, it remains to be demonstrated whether custom-designed superoscillatory waveforms can be synthesized in a practical manner conducive to imaging beyond the diffraction limit.

This present work aims to achieve two objectives: to elucidate the relationship between the aforementioned methods towards imaging beyond the diffraction limit, and to experimentally demonstrate sub-diffraction focusing by synthesizing a custom-designed superoscillatory waveform at a multi-wavelength image distance—10-fold increased from the image distances of evanescent-field-based imaging devices. In Section II, we begin by reviewing the physics behind the diffraction limit from a Fourier perspective. Upon this platform we then compare the phenomena of superlensing, superdirectivity and superoscillation. Subsequently, in Section III, we focus our attention on superoscillation as our method of choice to demonstrate sub-diffraction focusing at a multi-wavelength image distance. First we review our design formulation reported in previous works, then we describe the motivation towards an in-waveguide experiment and provide fabrication and operational details of our experimental apparatus. We then show results which represent a first experimental demonstration of custom-designed sub-diffraction focusing at a 4.8 wavelength imaging distance. Our ability to achieve sub-wavelength focusing in this extended imaging distance with a designer waveform distinguishes this work from [18], [19], in which randomness prohibits the prediction and design of the location of sub-wavelength foci, and the specification of the field profile

Manuscript received March 22, 2011; revised May 31, 2011; accepted June 16, 2011. Date of publication August 22, 2011; date of current version December 02, 2011. This work was supported in part by the Natural Science and Engineering Research Council of Canada (NSERC).

The authors are with the Rogers S. Sr. Dept. of Electrical and Computer Engineering, University of Toronto, Toronto, ON M5S 3G4, Canada (e-mail: alex.wong@utoronto.ca; gelefth@waves.utoronto.ca).

Color versions of one or more of the figures in this paper are available online at http://ieeexplore.ieee.org.

Digital Object Identifier 10.1109/TAP.2011.2165518

immediately surrounding the foci. Finally, we offer a brief discussion suggesting future directions to this work and potential areas of application.

II. Avenues to Sub-Diffraction Imaging

A. Diffraction Limit

Before we embark on a comparison of different methods of sub-diffraction imaging, it is helpful to review the physics behind the diffraction limit from a Fourier-transform perspective. Every electromagnetic waveform can be written as a composition of plane waves with varying transverse spatial frequencies (k_x) (for clarity we consider 2D wave propagation with x and z as the transverse and longitudinal directions respectively)

$$E(x,z) = \int_{-\infty}^{\infty} A(k_x) e^{-j(k_x x + k_z z)}\, dk_x = \int_{-\infty}^{\infty} S(k_x, z) e^{-jk_x x} dk_x \tag{1}$$

where we define

$$S(k_x, z) = A(k_x) e^{-jk_z z} \text{ where } k_z = -j\sqrt{k_x^2 - k_0^2} \tag{2}$$

as the plane-wave spectrum for $E(x,z)$, which is its Fourier transform in the k_x domain. The uncertainty principle forbids a function and its Fourier transform pair to simultaneously be localized [20]. In mathematical terms,

$$\Delta k_x \Delta x \geq C \tag{3}$$

where the constant C depends on the way in which the widths Δx and Δk_x are quantified. While this principle was made famous by Heisenberg in a quantum mechanical context, it also causes the diffraction limit for electromagnetic fields, in the following two different contexts.

Spatial Diffraction Limit: The evanescent components of an electromagnetic waveform (for which $|k_x| > |k_0| = (2\pi/\lambda); k_z \in I$) decay in the longitudinal direction and thus do not escape the evanescent near-field of an object or a device. As thus, only the propagating spectrum remains beyond the evanescent near-field of an imaging system. Hence the width of such a plane wave spectrum is limited to

$$-k_0 \leq k_x \leq k_0 \Rightarrow \Delta k_x \leq 2k_0 = 4\pi/\lambda. \tag{4}$$

In many imaging systems, geometrical limitations impose a finite aperture size, and hence prohibit one from accessing the entire spectrum of propagating waves. Imaging systems where propagation is limited to $|k_x| \leq k_{xm} < k_0$ is characterized by a numerical aperture $\mathrm{NA} = k_{xm}/k_0 = \sin\phi_m$, where ϕ_m is the maximum angle which a plane wave exiting the imaging system can form with the principal axis (z-axis). In such cases (4) becomes

$$\Delta k_x \leq 2k_{xm} = 4\pi(\mathrm{NA})/\lambda. \tag{4b}$$

The uncertainty principle translates this maximum width Δk_x into a minimum width Δx to which one can focus a propagating electromagnetic wave; this forms a measure for spatial resolution since such a focus can be viewed as a point spread function for more intricate imaging systems. Δx, obtained in this context, is called the Abbe diffraction limit or simply the diffraction limit. For most typical metrics of waveform width (3 dB width, peak to null width, etc.), and for numerical apertures approaching unity, the diffraction limit ranges from 0.4λ to λ.

Angular Diffraction Limit: In a different but related manifestation, diffraction limits the divergence angle of an electromagnetic beam emanating from a source, for example an antenna. The finite extent of the aperture of the source radiation (fixed Δx) sets a lower bound for Δk_x through the uncertainty principle. It is well known that in the far-field of an antenna, each propagating component k_x maps into a plane wave whose wave vector makes an angle θ with the positive x-axis (antenna axis), where

$$\theta = \cos^{-1}\left(\frac{k_x}{k_0}\right). \tag{5}$$

It is straightforward to show that this relation maps a spectral width k_x into a far-field angular beamwidth $\Delta\theta$ through the relation

$$\Delta\theta = 2\sin^{-1}\left(\frac{\Delta k_x}{2k_0 \sin\theta_{\mathrm{ctr}}}\right) \tag{6}$$

where $\Delta\theta$ denotes the beamwidth and θ_{ctr} denotes the beam direction. For small angular beamwidths, (6) simplifies to

$$\Delta\theta = \frac{\csc\theta_{\mathrm{ctr}}}{k_0}\Delta k_x. \tag{7}$$

Combining (7) with (3) yields

$$\Delta\theta\Delta x \geq C', \text{ where } C' = \frac{C\csc\theta_{\mathrm{ctr}}}{k_0} \tag{8}$$

which shows that a fixed aperture size leads to a lower bound for the emanating antenna beamwidth. This limitation will be referred to as the angular diffraction limit, or the diffraction limit for directivity.

In this paper, we use the term "sub-diffraction" to represent length scales or resolutions beyond the spatial or angular diffraction limit. Moreover, we use the term "sub-wavelength" to refer to length scales or resolution beyond the spatial (but not angular) diffraction limit. Also, we focus our discussion on the focusing problem, having already established its equivalency to the corresponding imaging problem.

B. Superlensing/Evanescent-Field-Based Focusing

The deployment of evanescent waves has been predominant in sub-diffraction imaging devices proposed thus far. The underlying idea is simple: including evanescent waves in the imaging process allows one to access a transverse spatial frequency spectrum much larger than twice the wave number (i.e., $\Delta k_x \gg 2k$). As a result, the uncertainty relation (3) becomes much less constraining on Δx, thus allowing one to obtain a much finer resolution. Near-field scanning schemes represent a simple

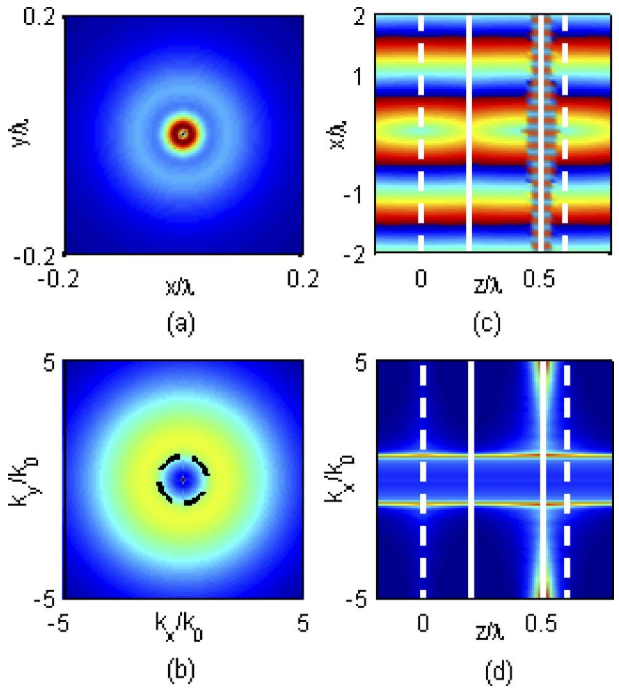

Fig. 1. Evanescent-field-based sub-diffraction imaging. (a) The field pattern at a plane 0.05 wavelength away from a z-directed small dipole is tightly localized to below $0.01\lambda^2$. (b) The corresponding spatial spectrum, showing large evanescent-wave content. The black dashed circle separates the propagating spectrum (inside) from the evanescent spectrum (outside). (c) Phase progression for a line source that is imaged by a superlens. Solid white lines denote the location of the superlens, while dash white lines denote the locations of the source (to the left of the lens) and image (to the right of the lens). (d) The corresponding spectral evolution, showing large evanescent field components near the output facet of the superlens.

way of employing evanescent waves for measurement purposes. Fig. 1(a) and (b) show the electric field amplitude and transverse spatial field spectrum at 0.05λ from a near-field scanning tip, showing that evanescent field components are present and essential for sub-diffraction near-field scanning. Metamaterial superlensing also achieves sub-diffraction resolution imaging due to a resonant enhancement of evanescent fields within a negative-index slab, which compensates for their decay in free space, and thereby increases the working image distance to up to quarter-wavelength in practice (limited mainly due to material losses). Fig. 1(c) and (d) show the phase progression and spectral amplitude distribution as a line source is refocused by a superlens. The abundance of evanescent waves at the output facet of the superlens confirms the participation of evanescent waves in sub-diffraction resolution image formation.

Since the proposal of the metamaterial superlens, other schemes have been conceived to employ evanescent waves in clever manners to focus or resolve waveforms beyond the diffraction limit. The metascreen [8] and the near-field focusing plate [9], [21] synthesize the electric field at the output facet of the device which will form a sub-wavelength focus at a predefined image distance. While these devices do not perform point-to-point sub-wavelength imaging in the same sense as the superlens, they can nonetheless form sub-wavelength foci which, if desired, can be used for imaging in a point-scan apparatus. In related developments, near-field gratings [4], [5], near-field scatterers [22] and the hyperlens [6], [7] are placed very close to the object, to convert evanescent fields into propagating ones and thus resolve them in the far-field.

The employment of evanescent waves within the image recording/formation process has indeed been proven effective towards achieving sub-wavelength resolution. However, this comes at a steep price of a constrained image distance. In near-field scanning setups, scan probes are often placed much less than a tenth of a wavelength away from the sample, where the field extending off the tip of the probe remains tightly localized. The metamaterial superlens typically operates with image distances ranging from a twentieth to a quarter of the wavelength. Beyond this distance, such a significant resonant enhancement is needed from the superlens that the achievable resolution quickly degrades due to dispersion [23] and various kinds of losses [23]–[25]. The same is true for all aforementioned imaging methods based on evanescent waves: they must necessarily be limited to the evanescent near-field either in their image distances (metascreens and focusing plates), or their object-to-device distances (near-field scatters, gratings and hyperlens). This fundamental limitation in working distance prevents superlensing from bringing sub-wavelength resolution to many applications.

C. Superdirectivity

Superdirectivity refers to the achievement of higher directivity than a similar-sized uniform aperture antenna, from which the emanating beam angle can be referred to as the angular diffraction limit. While it was traditionally believed that one can achieve the smallest beam angle with a uniform aperture antenna, Schelkunoff, in his seminal work in 1943, suggested otherwise. He proposed a theory whereby one can design current excitations on an antenna array such that the main beam can be arbitrarily squeezed without increasing overall antenna size. Fig. 2(a) shows current excitations from three arrays of isotropic antennas, all of overall length 2λ; Fig. 2(c) compares their beam patterns with that from a uniform antenna array. The angular diffraction limit is clearly overcome with these superdirective antennas.

Underlying Mechanism: The Fourier perspective clearly elucidates how the superdirective antenna overcomes the angular diffraction limit. Fig. 2(b) shows the transverse spatial spectra for array factors of the superdirective antennas displayed in Fig. 2(a). While they contain tight peaks and low sidelobes in the region of propagating waves ($|k_x| \leq k_0$), they also contain huge sidebands in the region of evanescent waves ($|k_x| > k_0$). Hence the superdirective array-factors have wide waveform widths in the transverse spatial frequency domain, which is in accordance to the uncertainty principle. However, as one maps the near-field spectrum into the antenna's far-field, only the propagation spectrum is mapped; evanescent waves are invisible to the far-field. In this manner, the narrow peaks in the propagating spectra map into the highly directive beams whose angular widths surpass the diffraction limit.

Superdirectivity and the Spatial Diffraction Limit: While it is well known that a superdirective antenna can focus the direction of electromagnetic radiation beyond the angular diffraction limit, one might speculate whether it can also be used for high-

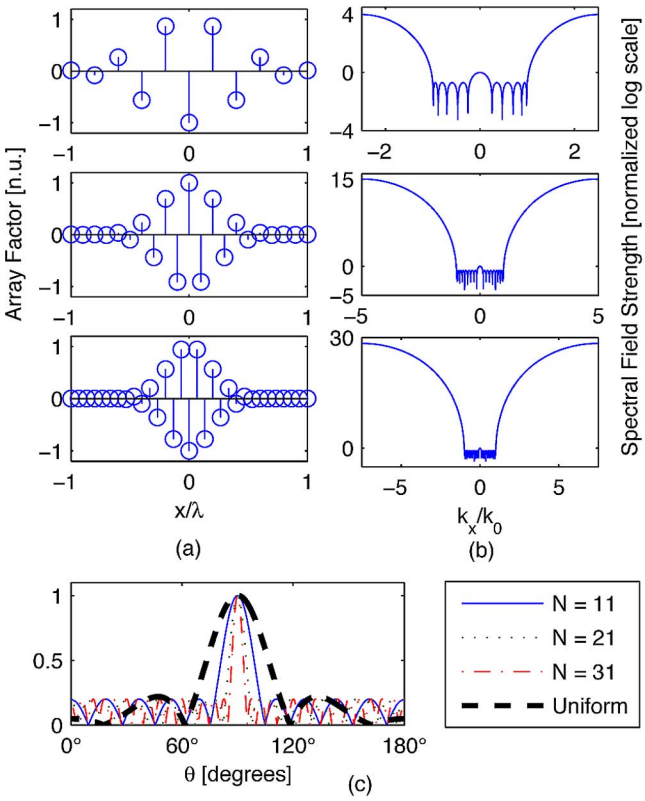

Fig. 2. (a) Array factors for 3 antennas arrays (of 11, 21 and 31 elements respectively) of length 2λ. (b) The corresponding spatial spectra, showing very high amplitude evanescent components. Here $|k_x/k_0| \leq 1$ represents the propagating spectrum. (c) The corresponding far-field angular distributions, compared to that of a uniform array.

resolution imaging beyond the spatial diffraction limit. Such speculation might stem from two observations: that the superdirective antenna has a large evanescent spectrum, and that the antenna beam angle can, at least conceptually, be arbitrarily squeezed in the antenna pattern. We now examine these two observations and show that they do not give superdirective antennas the ability to image beyond the spatial diffraction limit.

We begin with the first observation. It is indeed true that superdirective antennas contain large evanescent spectra, and that sub-wavelength field variations might be observed within its near-field, in similarity with previously discussed evanescent-field-based imaging devices. However, distinction must be made in the evanescent fields' "purpose of existence" in these two cases of sub-diffraction imaging: in near-field imaging schemes, evanescent-field-dominated near-field profiles perform the imaging, whereas for superdirective antennas, evanescent fields can be viewed as by-products of the antenna pattern design process, which become invisible in the regime where the image (the desired antenna pattern) is formed. Due to this difference in purpose of existence, evanescent waves present at the near-field of a superdirective antenna are not optimized for near-field sub-diffraction imaging purposes. Of course, one can alter the current excitations of a superdirective antenna to achieve near-field sub-wavelength imaging. However in this case the array antenna ceases to become superdirective, hence the device becomes a sub-wavelength spaced antenna array used for evanescent-field-based sub-wavelength imaging, similar to [8].

We continue to examine the second observation, which can be cast as the following question: can a superdirective antenna be designed to form a sub-wavelength far-field focal spot? The antenna far-field is nominally described by the relation,

$$r_{\mathrm{ff}} \geq \frac{2D^2}{\lambda} \tag{9}$$

where D represents the overall antenna size. At this distance the spatial beamwidth is given by

$$\Delta x = r_{\mathrm{ff}} \Delta\theta \geq \frac{2D^2 \Delta\theta}{\lambda}. \tag{10}$$

Since, in principle, the beam angle $\Delta\theta$ of a superdirective antenna can be arbitrarily squeezed without changing the antenna size D, one might suppose the spatial beamwidth can also be arbitrarily squeezed by taking $\Delta\theta$ to zero. This is, however, in direct contradiction with (8). As noted in [26], the rapid spatial phase variations in a superdirective antenna require better phase agreement between waves reaching an observation point from the central part of the antenna, and waves reaching the same point from the edge of the antenna. This intolerance to phase difference renders the traditional Rayleigh distance—as recorded on the right-hand side of (9)—inadequate; instead one needs to travel even further from the antenna before the far-field antenna pattern is formed. Hence, as one increases the gain of the superdirective antenna, one decreases $\Delta\theta$, but at the same time increases r_{ff}. As a result Δx does not get arbitrarily squeezed. This fact is illustrated in Fig. 3, which shows field evolutions from three superdirective antennas of lengths 5λ, 2λ and λ, but nevertheless are designed to have similar far-field beam angles (hence they have different degrees of superdirectivity). If we qualitatively define the onset of the far-field as the place where the first sidelobe decreases to half the field amplitude of the main beam, then we see from Fig. 3 that for these three antennas the far-field region begins at around 20λ away from the antenna. This clearly shows the inapplicability of (9); furthermore, it shows that increasing an antenna's superdirective gain also pushes out its far-field regime. Fig. 4 shows the onset of the far-field, as well as the spatial width (the electric field full width at half maximum) of superdirective antennas of varying directivities. We see from this figure that squeezing an antenna's angular beamwidth does not necessarily squeeze its spatial dimensions in the far-field; it might actually increase it. This analysis is in agreement with the uncertainty principle: one should not be able to obtain sub-wavelength field localization with a waveform limited to propagating waves. We are thus left to conclude that while a superdirective antenna overcomes the angular diffraction limit, it does not also overcome the spatial diffraction limit.

D. Superoscillation

Whereas the superdirective antenna fails to bring propagating waves into a sub-wavelength focus, superoscillations can do the job. Superoscillation is the phenomenon whereby a waveform locally oscillates faster than its highest constituent frequency component. As a result, combining a range of these waveforms

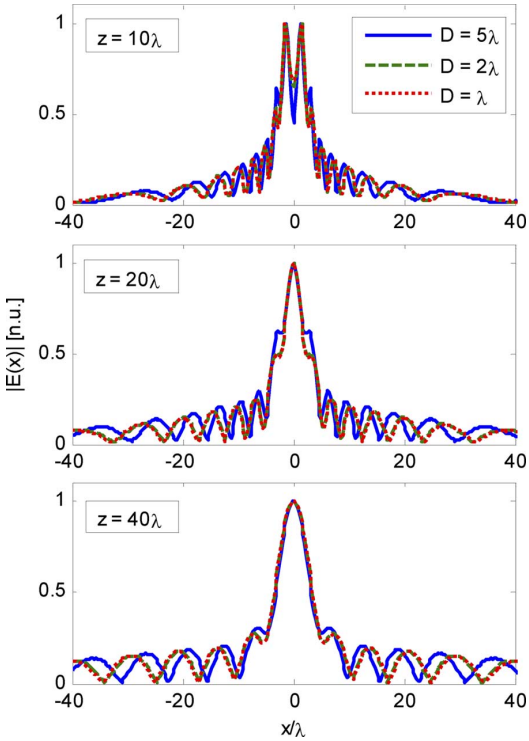

Fig. 3. Field evolutions from three antenna arrays, of electrical sizes 5λ, 2λ and λ respectively, which are designed to have similar far-field antenna patterns. The antenna axis is at $z = 0$.

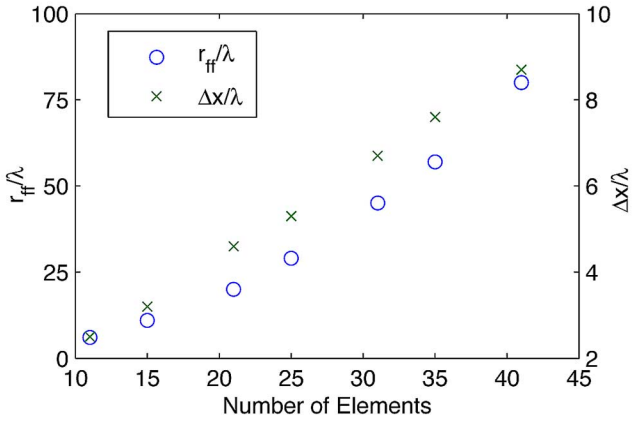

Fig. 4. A plot of the far-field distance, and the corresponding beamwidth at that distance, for Chebyshev superdirective antennas with varying numbers of elements, with fixed electrical lengths of 2λ.

effectively forms a spectrum which is locally widened, which then allows the formation of foci and other wave patterns with sub-diffraction spatial features. However, along with the desired superoscillatory features come high energy sidebands outside the region of superoscillation, the energy for which varies polynomially with the superoscillatory region's apparent spectral width, and exponentially with its duration [27].

A simultaneous glance at a superoscillation profile in the spatial and spatial frequency domains proves sufficient for one to understand how superoscillations occur. While the superoscillatory waveform occupies a limited spectral width—namely the region of propagating waves, they can generate arbitrarily fast oscillations and narrow peaks within a certain stretch of the spatial domain, as long as one tolerates high energy sidebands to occur outside the spatial stretch. This process is exactly analogous to superdirectivity: only now the spatial (x) and spatial frequency (k_x) domains are flipped; moreover, without an equivalent of the far-field transformation process which occurs for superdirectivity, the high energy sidebands remain visible [28]. Nonetheless, in this manner one can generate a sub-wavelength focus employing propagation waves, and thus extend spatial sub-diffraction imaging capabilities to working distances beyond the evanescent near-field of the object and the imaging device. In the following we report our efforts towards demonstrating superoscillatory sub-diffraction focusing at five wavelengths away from a source.

III. Superoscillatory Sub-Wavelength Focusing at the Multi-Wavelength Range

A. Design Formulation

In the above section we have shown the dual relationship between the phenomena of superdirectivity and superoscillation. In a previous work, we leveraged this duality to design superoscillation signals by adapting established techniques for superdirective antenna design [28]. For completeness we briefly review our method here before proceeding to report experimental results. We refer interested readers to our previous work [28] for finer details.

We post our problem in reverse: first we specify the desired superoscillatory waveform in the image plane, then we back-propagate the desired field pattern to determine the source excitation required, and finally we synthesize the desired source excitation. For the first procedure, we expand our target waveform into Tschebyscheff polynomials [8], [9] to determine the set of zeros (z_n) in the plane of $z = e^{-jx\Delta k}$, such that upon a transformation to the x-domain, we would obtain an image waveform with the narrowest central peak width, along with constant sidelobes at 20% the central peak field strength (4% intensity) for a region of half wavelength on both sides of the peak. After z_n is obtained, multiplicative expansion on a product of these roots reveals the image waveform $E_{\text{img}}(x)$ in a formation akin to the array factor in antenna array design. Thereafter a Fourier transform reveals the discrete spatial spectrum $\tilde{E}_{\text{img}}(k_x)$

$$E_{\text{img}}(x) = Ca_{N-1}\prod_{n=1}^{N-1}(z - z_n) = C\sum_{n=0}^{N-1} a_n z^n \qquad (11)$$

where $z = e^{-jx\Delta k}$, $C = e^{-jxk_{x0}}$

$$\tilde{E}_{\text{img}}(k_x) = \sum_{n=0}^{N-1} a_n \delta(k_x - n\Delta k - k_{x0}). \qquad (12)$$

Here a_n is the weighting of the n'th delta function, N is the number of delta functions in the spectral domain, Δk is the spacing between delta functions in the spectral domain, k_{x0} is the transverse frequency of the first (most negative) delta function and C is a phase constant which simplifies the notation in (12). We choose the latter three parameters such that all harmonics (or all delta functions in the spatial spectrum) lie within the propagation region. This allows us to back propagate these

harmonics to the source location at a multi-wavelength distance s away, and obtain the source spatial spectrum $\tilde{E}_{\rm src}(k_x)$, inverse Fourier transforming which gives the source field profile $E_{\rm src}(x)$.

$$\tilde{E}_{\rm src}(k_x) = \tilde{E}_{\rm img}(k_x)e^{+jk_z s} \Rightarrow b_n = a_n e^{+jk_z s}$$
$$k_z = -j\sqrt{k_0^2 - k_0^2} \tag{13}$$
$$E_{\rm src}(x) = \frac{1}{2\pi}\sum_{n=0}^{N-1} b_n e^{j(k_{x0}+n\Delta k)x}. \tag{14}$$

When one chooses to synthesize this source field profile with an array of sources, the source spatial spectrum can be viewed as the spatial spectrum of the individual element, multiplied by that of the array. As such the spatial spectrum of the array would be given by

$$\tilde{E}_{\rm array,src}(k_x) = \frac{\tilde{E}_{\rm src}(k_x)}{\tilde{E}_{\rm elem}(k_x)} = \sum_{n=0}^{N-1} \frac{b_n \delta(k_x - n\Delta k - k_{x0})}{\tilde{E}_{\rm elem}(k_{x0}+n\Delta k)}. \tag{15}$$

Adequately sampling the inverse Fourier transform of $\tilde{E}_{\rm array,src}(k_x)$ will give the desired source excitation coefficients.

B. Waveguide Implementation

Motivation: In achieving sub-wavelength resolution it is essential to employ an imaging device with a high-numerical aperture (NA), such that the working spatial spectrum covers as much of the propagating region as possible. However, to obtain a high NA with an image distance in the multi-wavelength range, one would require an imaging device with a lateral aperture on the order of tens of wavelengths. Such a large electrical size, along with the corresponding large number of array elements, makes it inconvenient to demonstrate microwave superoscillation in free-space. On the other hand, a rectangular waveguide is an ideal platform for demonstrating microwave superoscillation. The $\rm TE_{p0}$ mode of a rectangular waveguide has a transverse spatial frequency given by

$$k_{xp} = \frac{p\pi}{w} \tag{16}$$

where w denotes the width of the waveguide in x-direction. Since these waveguide modes space uniformly in the k_x domain, they form a good candidate for synthesizing the source spectrum (13): one only needs to appropriately excite them to generate the desired source spectrum, which will then propagate into the desired superoscillation profile. In an equivalent view, the walls of a rectangular waveguide act as mirrors which image the source to mimic an infinite array. Hence with this platform, one can access the entire propagating spectrum and perform sub-wavelength focusing with several source elements. This makes for a relatively compact device. With these considerations in mind, we proceed to design and demonstrate a sub-wavelength superoscillatory focus at the multi-wavelength range in a waveguide environment.

Design: Here we outline the design parameters for designing our sub-wavelength superoscillatory waveform. We will employ

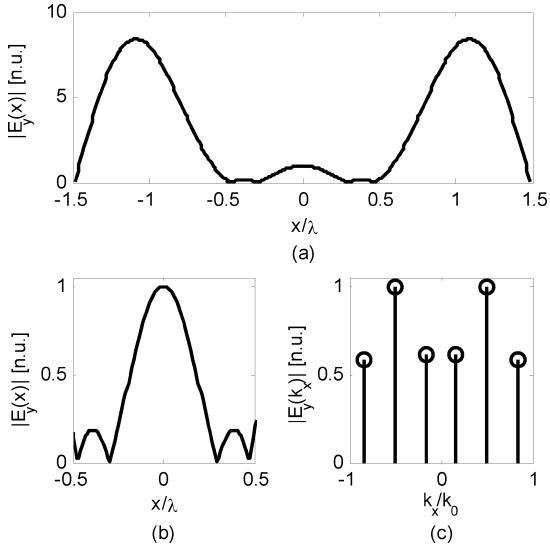

Fig. 5. (a) Superoscillatory image waveform across a 3λ (half-period) cross-section. (b) A close up of (a) in the design region of $x \in [-\lambda/2, \lambda/2]$. (c) A plot of the corresponding spatial spectral amplitudes.

$N = 6$ spectral lines in our design, which gives us freedom to place $N - 1 = 5$ zeros in our design procedure. We place 4 zeros to generate the focus as explained in the previous section, and place the remaining zero at $Z_5 = -1$ to align an electric field null point with the waveguide sidewalls.

Substituting these parameters into (11) and (12) gives the superoscillatory image waveform in Fig. 5(a). A close up on the design region is shown in Fig. 5(b), and the corresponding spatial spectrum is shown in Fig. 5(c).

We proceed to design an imaging device that produces this waveform from a distance $s = 5\lambda$ away, as depicted in Fig. 6(a). We find $E_{\rm src}(x)$ using (13) and (14), then synthesize it with an array of current line sources, placed at half wavelength intervals and embedded within a rectangular waveguide. The TE10, TE30 and TE50 waveguide modes form the desired harmonics depicted in Fig. 5(c). We use a waveguide with a width of $w = 3\lambda$ in the x-direction, which corresponds to choosing

$$\Delta k = \frac{2\pi}{3\lambda} = \frac{k_0}{3};\ k_{x0} = -\frac{5\pi}{3\lambda} = -\frac{5k_0}{6}. \tag{17}$$

This ensures the existence of the TE50 mode, but cuts off higher-order modes. The field emanating from a line source is described by a zero order Hankel function of the second kind, for which the corresponding spatial spectrum is [29]

$$\tilde{E}_{\rm elem}(k_x) = \frac{2}{k_z} = \frac{2j}{\sqrt{k_x^2 - k_0^2}}. \tag{18}$$

Substituting (18) into (15) gives

$$\tilde{E}_{\rm array,src}(k_x) = \sum_{n=0}^{N-1} b'_n \delta(k_x - n\Delta k - k_{x0})$$
$$\text{where } b'_n = -\frac{jb_n\sqrt{(k_{x0}+n\Delta k)^2 - k_0^2}}{2} \tag{19}$$
$$\tilde{E}_{\rm array,src}(x) = \frac{1}{2\pi}\sum_{n=0}^{N-1} b'_n e^{j(k_{x0}+n\Delta k)x}. \tag{20}$$

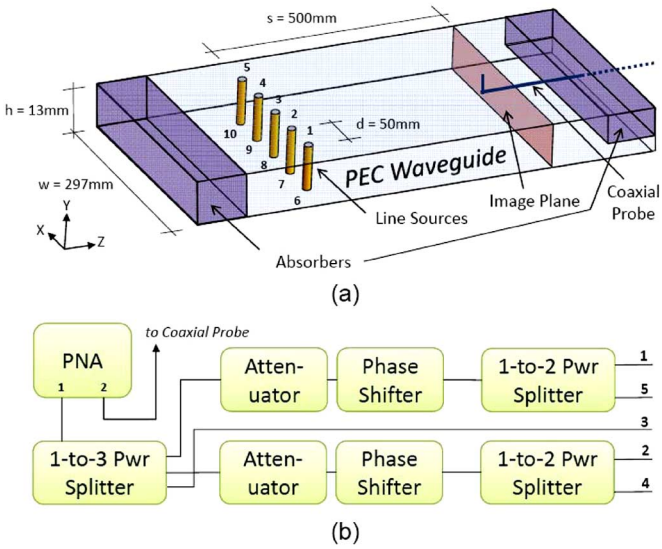

Fig. 6. (a) A schematic of the experimental setup. (b) A diagram of the feed network.

TABLE I
CURRENT EXCITATION COEFFICIENTS NEEDED TO GENERATE A SUB-WAVELENGTH FOCUS AT AN IMAGE DISTANCE OF 5λ.

Element	h[n]	Adjusted h[n]
1	0.2930 ∠ -2.769 rad	0.3272 ∠ -2.845 rad
2	0.2732 ∠ -1.044 rad	0.3548 ∠-1.127 rad
3	1	1
4	0.2732 ∠ -1.044 rad	0.3548 ∠-1.127 rad
5	0.2930 ∠ -2.769 rad	0.3272 ∠ -2.845 rad

Finally, we sample $E_{\text{array,src}}(x)$ at half wavelength intervals to obtain the required line source excitation coefficients h[n], which we have tabulated in Table I.

Fabrication and Experimentation: We bent a $1/8''$ (3.2 mm) sheet of stainless steel into a waveguide section of width 297 mm, height 12 mm and length 1 m. Due to a fabrication error, the waveguide width is slightly narrowed from the intended 300 mm, which would represent 3λ for the experimental frequency of 3 GHz. To reflect this change, we modify our calculations above and obtain adjusted values for h[n], which are also tabulated in Table I.

We embedded five metallic posts (1.2 mm diameter) spaced at 50 mm each along the x-direction to form an array of line sources 200 mm into the $-$z end of the waveguide. Each post is formed by connecting two inner conductors which extrude from their respective SMA receptacles which are welded above the top and beneath the bottom waveguide walls. Holes of sufficient sizes are drilled through the top and bottom waveguide walls at the location of the posts, such that the inner conductors, when fitted through from both sides, connect without forming electrical contact with the waveguide. The SMA receptacles provide access ports. In our experiment, we use them to feed current into the metallic posts and to monitor their current levels. We feed the aforementioned array of line sources using the feed network schematized in Fig. 6(b). The microwave source originates from port 1 of a programmable network analyzer (PNA),

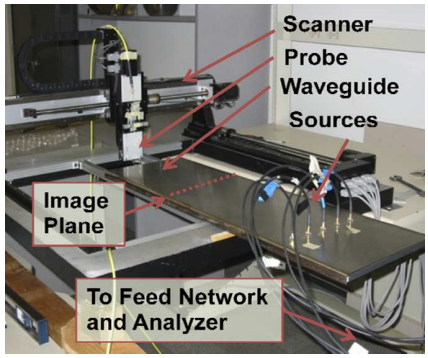

Fig. 7. A photograph showing the experimental apparatus.

and splits into three signal paths through a 1-to-3 power splitter. One output path from this power splitter directly feeds into port 3 of the waveguide (see Fig. 6(a) for port enumeration); outputs from the other two paths each go through a variable attenuator and a variable phase shifter, then get power divided and fed into ports 1 and 5, and 2 and 4. In this manner, we obtain freedom to tune the complex current inputs into ports 1 to 5.

Since we operate with closely spaced antenna elements embedded in a waveguide environment, we need to account for mutual coupling effects amongst our antenna elements. To accomplish this, we monitor fields coupled into ports 6 to 10 by connecting these ports sequentially to port 2 of our PNA. Since the coupled currents are, by and large, proportional to the currents on the posts, we tune our feed network such that the set of values S_{i1}/S_{81} for i $=$ 6 to 10 match those for h[n] (as listed in Table I) for the experimental frequency 3 GHz. This tuning procedure allows us to account for mutual coupling, and thus synthesize the desired current excitation on the source array.

Fig. 7 shows a photograph of the experimental apparatus. With the aforementioned feeding network we drive predesigned currents into the source array, and thus generate the TE10, TE30 and TE50 waveguide modes in appropriate proportions. (The TE20 and TE40 modes are rejected due to excitation symmetry.) We place microwave absorbers at the ends of the waveguide to quench reflected components, but leave a small gap at the end in the $+$z direction, through which we insert a coaxial cable probe to measure the y-directed electric field at the image region 500 mm (5λ) away from the source.

C. Simulation and Experimental Results

With the source located at $z = 0$ mm, we scan the probe to measure the electric field at a series of cross-sections from $z = 450$ mm to $z = 530$ mm, with spacing of 10 mm. We scan the probe across each cross-section from $x = -130$ mm to $x = 130$ mm at step sizes of 2.5 mm. We leave a space of 18.5 mm on either side of the waveguide cross-section to avoid colliding the probe with the waveguide walls. The measured electric field profile across this region is shown in Fig. 8(c).

We compare our measurement with full-wave simulation results obtained using Ansoft HFSS. In our simulation, we provide wave port excitation to SMA connectors, which in turn couple currents into the metallic posts, thus forming the source array. Here, we account for mutual coupling effects by setting the wave port excitation weights $w[n]$ as

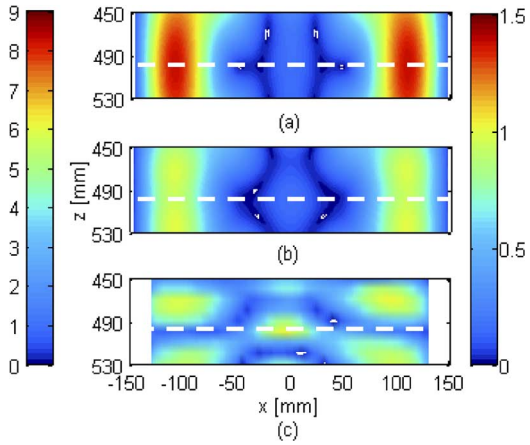

Fig. 8. Electric field profiles near the image plane $z = 500$ mm (denoted by white dash lines). (a) Simulation with absorbers covering the entire waveguide end facets. (b) Simulation with a partial gap in the absorber at the +z end of the waveguide (see Fig. 6 for pictorial depiction. (c) Measured electric field magnitude. The color bar to the left applies to (a) and (b); the one to the right applies to (c).

$$w[n] = S_{\text{mc}}^{-1} h[n] = \begin{bmatrix} S_{61} & S_{62} & S_{63} & S_{64} & S_{65} \\ S_{71} & S_{72} & S_{73} & S_{74} & S_{75} \\ S_{81} & S_{82} & S_{83} & S_{84} & S_{85} \\ S_{91} & S_{92} & S_{92} & S_{94} & S_{95} \\ S_{10,1} & S_{10,2} & S_{10,3} & S_{10,4} & S_{10,5} \end{bmatrix}^{-1} \begin{bmatrix} h_1 \\ h_2 \\ h_3 \\ h_4 \\ h_5 \end{bmatrix} \tag{21}$$

where S_{mc} describes a selected portion of the simulated 10-port S-parameter from which we distill information on mutual coupling effects (again, see Fig. 6(a) for port enumeration). The source array excites relevant waveguide modes in appropriate proportions, which are guided through the stainless steel waveguide, and terminated by perfect matching layers (PMLs). These PML blocks span the entire cross-section of the waveguide, and are placed at the same longitudinal locations as the absorbers in the experiment. The resulting electric-field magnitude is plotted in Fig. 8(a). It displays near-perfect agreement with an analytical field magnitude calculation of the interference of prescribed portions of the TE10, TE30 and TE50 modes. The sub-diffraction central peak, as well as the high energy sidebands, are visible across this entire region; the fixed ripple sidelobe region also appears around the designed image plane at $z = 500$ mm.

To reconcile the apparent difference between the simulated and experimental results (Fig. 8(a) and (c)), we run a modified simulation where we introduce a 6 mm gap in the y-direction for the PML situated at the end facet of the waveguide, from whence our coaxial cable probe is inserted in the experiment. Fig. 8(b) shows the electric-field magnitude of this modified simulation. Here, the presence of a reflected wave generates observable standing-wave patterns. As a result, the sideband amplitude is decreased—particularly at $z = 500$ mm—and the central peak is widened. In this spirit, we see that Fig. 8(c) resembles Fig. 8(b) in that all major peaks in Fig. 8(b) are observed

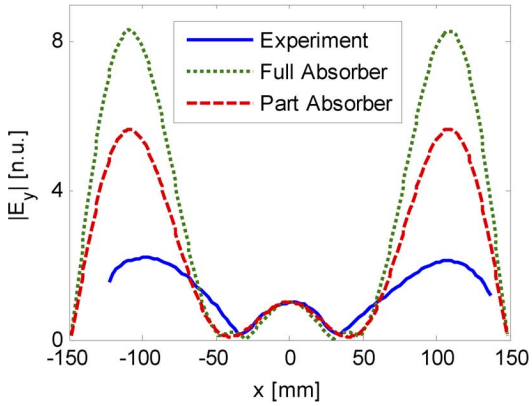

Fig. 9. A comparison on the measured and simulated superoscillatory foci at the image plane. The simulated field profiles are taken at the design image plane $z = 500$ mm, while the measured field profile is taken at z = 480 mm.

in Fig. 8(c). However, the seemingly more significant reflected wave components cause a sideband cancellation at $z = 500$ mm, producing a central peak which becomes much more pronounced in amplitude, but no longer sub-wavelength. Nevertheless, a sub-wavelength pattern is formed in the immediate vicinity at $z = 480$ mm; we will examine the experimental focal quality at this distance in the following figures. Some experimental factors which lead to reflected waves, or otherwise disturb the superoscillatory wave interference pattern, include the intrusion of the coaxial cable probe, the receiving characteristic of the small, but finite-sized, probe tip, rounded waveguide corners, and slight asymmetry in feed network distribution and source array construction. Notwithstanding, the field measured at cross-sections slightly before the designed imaging distance remains superoscillatory despite interference with reflected waves.

Figs. 9 and 10 plot and compare the measured and simulated waveform cross-sections at $z = 500$ mm (5λ) and a nearby plane $z = 480$ mm (4.8λ). Simulation with a full (PML) absorber at the +z end of the waveguide leads to a superoscillation focus with an electric field full-width-half-maximum (FWHM) of 37 mm (0.37λ). This electric field profile is in exact agreement with the target waveform, apart from slight deviations surrounding the outer pair of nulls. However, when we employ the partial absorber at the +z end of the waveguide, the image profile widens to a FWHM of 45 mm (0.45λ). Whereas reflected wave components and slight asymmetry in the +x direction obscure our superoscillatory focusing measurement at $z = 500$ mm, the measured electric field cross-section at $z = 480$ mm (4.8λ) clearly demonstrates superoscillatory behavior. This profile is plotted in Figs. 9 and 10 for comparison purposes. Here the electric field FWHM of the central peak is squeezed to 45 mm (0.45λ)—comparable to the partial absorber simulation and at 75% of the diffraction limit of 61 mm (0.61λ), formed from a uniform, in-phase superposition of all symmetric modes within the waveguide. Even though experimental imperfections prevented us from obtaining a region of low sidelobe ripples, we have nevertheless successfully demonstrated superoscillatory sub-diffraction focusing at a multi-wavelength image distance.

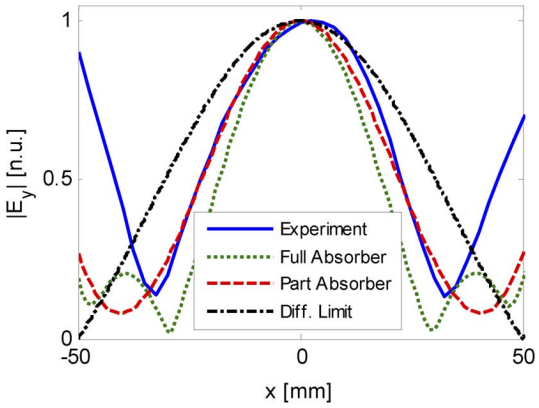

Fig. 10. A close up of Fig. 9, comparing the measured and simulated superoscillatory foci across the design interval. The diffraction-limited focus in this waveguide environment is also included for comparison. As in Fig. 9, the simulated field profiles are taken at $z = 500$ mm, while the measured field profile is taken at $z = 480$ mm.

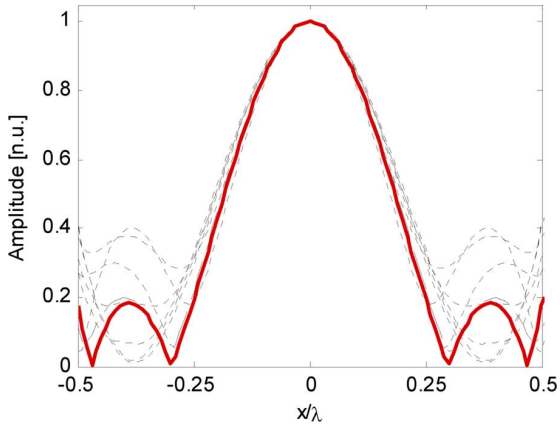

Fig. 11. Sensitivity of the superoscillatory focus. The red curve shows the design superoscillatory focus, while dotted curves show typical electric field amplitude distributions when a 2.5% error is introduced in the waveguide mode weightings.

D. Discussion

We begin our discussion with a comment on sensitivity. It has been well known that sensitivity issues prevent superdirective antennas from arbitrarily squeezing the width of a beam emanating from an antenna. We have therefore tested the sensitivity of the superoscillatory waveform we generated, to confirm that reasonable levels of spot size reduction can be achieved with tolerances which are practical for implementation. To characterize the sensitivity of our proposed method, we vary the excitation coefficients by adding to each waveguide mode a randomly phased white Gaussian component with mean amplitude 2.5% of the strongest excitation coefficient. Typical resulting waveforms are plotted in Fig. 11. Despite the appearance of an uneven and increased sidelobe level, our achieved subwavelength focal width is unaffected by this level of perturbation. A similar analysis on the waveguide excitation currents has been conducted in [28], where it was found that a precision level of 1% is sufficient to obtain the desired sub-diffraction focus. As this required level of precision was met by our device, we believe degradations observed in Figs. 8–10 are not caused by the sensitivity of the superoscillatory waveform, but rather due to the reasons outlined in the previous section. In practice, the precise excitation of current elements (and hence the relevant waveguide modes) comes easier for superoscillatory waveforms than it does for superdirective antennas, since no radiative energy is stored, and since relatively wide antenna spacings $(\geq\lambda/2)$ reduce the significance of mutual coupling. Hence, the aforementioned level of precision is by no means stringent in current imaging systems. Thus we believe superoscillatory sub-diffraction focusing can be implemented in a wide range of practical platforms.

We proceed to comment on the regime in which we performed sub-diffraction focusing. Unlike evanescent-field-based imaging devices, we have formed a sub-diffraction focus far beyond the region of existence and dominance of evanescent waves. However, the focus formed does not exist in the far-field either—in the sense that our sub-diffraction focal distribution is not a scaled copy of its spatial spectrum, hence the Fraunhofer approximation does not apply. Rather our sub-diffraction focus lies in the radiating near-field—where only radiating waves exist, but the dynamics of their interference determines the overall spatial waveform. Notwithstanding, that the domain of focus formation is not in the far-field should not be seen as a limitation. While we have experimentally demonstrated focusing at 4.8 wavelengths (480 mm), the radiating near-field can extend many-fold beyond this distance to cover practical ranges conducive to many applications.

We now discuss the waveguide environment in which we have performed superoscillatory sub-diffraction focusing. Indeed, we have demonstrated, for ease of experimentation, superoscillatory sub-wavelength focusing in a waveguide environment. However, our design formulation can be readily used for sub-wavelength focusing in a free-space environment. Waveguide walls in our experiment serve as mirrors for the source electric distribution. Hence they can be extended to any integral multiples of the waveform's spatial period (odd multiples for anti-mirrors), as long as the source distribution is also extended. In the limit of infinite extension, the waveguide solution converges to a free-space solution. Moreover, even with a finite extension, the waveguide cross-section can be enlarged at will to contain the object which is to be imaged. This finite extension renders the waveguide environment practical for imaging implementations at microwave frequencies.

Finally, we discuss the possibility of multi-dimensional superoscillatory sub-diffraction focusing. Although in this work we demonstrate sub-wavelength focusing in only one direction, an extension to multi-dimensional focusing is very conceivable—because a superoscillation is but a special superposition of propagating waves. Extension to 2D focusing in the waveguide environment is conceptually straightforward: one only needs to excite the waveguide with a 2D array, and tune the waveguide height to also allow the propagation of modes with y-directed oscillations. Excitation weightings can be readily determined by our proposed method, treating a 2D array as a y-directed array where each element is in itself an x-directed array. Thus with the incorporation of a more elaborate feeding network one can perform 2D sub-wavelength focusing with the waveguide environment proposed in this work.

It has been shown that evanescent-field-based focusing devices cannot form a 3D sub-diffraction focus, on grounds of an inevitable violation of the consistency relation [30]. This limitation, however, does not restrict the formation of superoscillatory 3D sub-diffraction foci, since superoscillatory waveforms can be formed by the sole interference of propagating waves. The unique ability to form a 3D sub-wavelength focus, combined with the ability to form such a focus at multi-wavelength distances, make superoscillatory sub-wavelength focusing attractive to a wide range of imaging and sensing applications.

IV. Conclusion

In this work, we have elucidated the difference among evanescent-field-based focusing, superdirectivity and superoscillation. In particular, we have shown that superdirectivity and superoscillation are dual phenomena in the spatial and spatial frequency domains. This property gives superoscillation the potential to overcome the spatial diffraction limit—to form a sub-wavelength focus with propagating waves. Realizing this as the avenue to push sub-wavelength focusing capabilities to working distances far beyond the evanescent near-field, we have formulated a proof-of-principle design to perform superoscillation-based 1D sub-wavelength focusing in a waveguide environment, and presented corresponding results from full-wave simulations and experimental measurements. We have experimentally achieved superoscillatory sub-wavelength focusing to 0.45λ electric field FWHM (75% of the diffraction limit) at a distance 4.8λ from the source—an order of magnitude increase from sub-wavelength focusing schemes with evanescent-field-based devices. While we have demonstrated 1D sub-wavelength focusing in a waveguide environment, our formulation can be extended to multi-dimensional sub-wavelength focusing in waveguide or free-space environments in conceptually straightforward manners. We believe the ability to form a sub-wavelength focus at a working distance much longer than the evanescent near-field regime could become very attractive for high-resolution imaging and sensing applications.

References

[1] E. H. Synge, "A suggested method for extending microscopic resolution into the ultra-microscopic region," *Philos. Mag.*, vol. 6, pp. 356–362, Aug. 1928.

[2] V. G. Veselago, "The electrodynamics of substances with simultaneously negative values of eps and mu," *Sov. Phys. Usp.*, vol. 10, pp. 509–514, Jan. 1968.

[3] J. B. Pendry, "Negative refraction makes a perfect lens," *Phys. Rev. Lett.*, vol. 85, no. 18, pp. 3966–3969, Apr. 2000.

[4] V. Eckhouse, Z. Zalevsky, N. Konforti, and D. Mendlovic, "Subwavelength structure imaging," *Opt. Eng.*, vol. 43, no. 10, pp. 2462–2468, Oct. 2004.

[5] Z. Liu, S. Durant, H. Lee, Y. Pikus, N. Fang, Y. Xiong, C. Sun, and X. Zhang, "Far-field optical superlens," *Nano Lett.*, vol. 7, no. 2, pp. 403–408, Feb. 2007.

[6] A. Salandrino and N. Engheta, "Far-field subdiffraction optical microscopy using metamaterial crystals: Theory and simulations," *Phys. Rev. B*, vol. 74, p. 075103, Aug. 2006.

[7] Z. Jacob, L. V. Alekseyev, and E. Narimanov, "Optical hyperlens: Far-field imaging beyond the diffraction limit," *Opt. Express*, vol. 14, no. 18, pp. 8247–8256, Sep. 2006.

[8] L. Markley, A. M. H. Wong, Y. Wang, and G. V. Eleftheriades, "Spatially shifted beam approach to subwavelength focusing," *Phys. Rev. Lett.*, vol. 101, pp. 113–901, Sep. 2008.

[9] A. Grbic, L. Jiang, and R. Merlin, "Near-field plates: Subdiffraction focusing with patterned surfaces," *Science*, vol. 320, pp. 511–513, Apr. 2008.

[10] R. Gordon, "Proposal for superfocusing at visible wavelengths using radiationless interference of a plasmonic array," *Phys. Rev. Lett.*, vol. 102, pp. 207–402, May 2009.

[11] G. V. Eleftheriades and A. M. H. Wong, "Holography-inspired screens for sub-wavelength focusing in the near field," *IEEE Microwave Wireless Compon. Lett.*, vol. 18, pp. 236–238, Apr. 2008.

[12] S. A. Schelkunoff, "A mathematical theory of linear arrays," *Bell Syst. Tech. J.*, vol. 22, pp. 80–107, Jan. 1943.

[13] Y. Aharonov, J. Anandan, S. Popescu, and L. Vaidman, "Superpositions of time evolutions of a quantum system and a quantum time-translation machine," *Phys. Rev. Lett.*, vol. 64, pp. 2965–2968, Jun. 1990.

[14] M. V. Berry, "Faster than Fourier," in *Quantum Coherence and Reality: In Celebration of the 60th Birthday of Yakir Aharonov*, J. S. Anandan and J. L. Safko, Eds. Singapore: World Scientific, 1994, pp. 55–65.

[15] M. V. Berry, "Evanescent and real waves in quantum billiards and Gaussian beams," *J. Phys. A: Math. Gen.*, vol. 27, pp. L391–L398, Jun. 1994.

[16] P. J. S. G. Ferreira, A. Kempf, and M. J. C. S. Reis, "Construction of Aharonov-Berry's superoscillations," *J. Phys. A: Math. Gen.*, vol. 40, pp. 5141–5147, May 2007.

[17] F. M. Huang and N. I. Zheludev, "Super-resolution without evanescent waves," *Nano Lett.*, vol. 9, pp. 1249–1254, Jan. 2009.

[18] F. M. Huang, N. Zheludev, Y. Chen, and F. J. G. De Abajo, "Focusing of light by a nanohole array," *Appl. Phys. Lett.*, vol. 90, p. 091119, Feb. 2007.

[19] M. R. Dennis, A. C. Hamilton, and J. Courtial, "Superoscillation in speckle patterns," *Opt. Lett.*, vol. 33, pp. 2976–2978, Dec. 2008.

[20] G. B. Folland and A. Sitaram, "The uncertainty principle: A mathematical survey," *J. Fourier Analy. Applicat.*, vol. 3, pp. 207–238, May 1997.

[21] R. Merlin, "Radiationless electromagnetic interference: Evanescent-field lenses and perfect focusing," *Science*, vol. 317, pp. 927–929, Aug. 2007.

[22] G. Lerosey, J. Rosny, A. Tourin, and M. Fink, "Focusing beyond the diffraction limit with far-field time reversal," *Science*, vol. 23, pp. 1120–1122, Feb. 2007.

[23] R. Marqués and J. Baena, "Effect of losses and dispersion on the focusing properties of left-handed media," *Microw. Opt. Technol. Lett.*, vol. 41, pp. 290–294, May 2004.

[24] D. R. Smith, D. Schurig, M. Rosenbluth, S. Schultz, S. A. Ramakrishna, and J. B. Pendry, "Limitations on subdiffraction imaging with a negative refractive index slab," *Appl. Phys. Lett.*, vol. 82, pp. 1506–1508, Mar. 2003.

[25] A. Grbic and G. V. Eleftheriades, "Practical limitations of subwavelength resolution using negative-refractive-index transmission-line lenses," *IEEE Trans. Antennas Propag.*, vol. 53, pp. 3201–3209, Oct. 2005.

[26] A. C. Marvin, A. P. Anderson, and J. C. Bennett, "Inadequacy of the Rayleigh range criterion for superdirective arrays," *Electron. Lett.*, vol. 12, pp. 415–416, Aug. 1976.

[27] P. J. S. G. Ferreira and A. Kempf, "Superoscillations: Faster than the Nyquist rate," *IEEE Trans. Signal Process.*, vol. 54, pp. 3732–3740, Oct. 2006.

[28] A. M. H. Wong and G. V. Eleftheriades, "Adaptation of Schelkunoff's superdirective antenna theory for the realization of superoscillatory antenna arrays," *IEEE Antennas Wireless Propag. Lett.*, vol. 9, pp. 315–318, Apr. 2010.

[29] F. Oberhettinger, *Tables of Fourier Transforms and Fourier Transforms of Distributions*. Berlin, Germany: Springer-Verlag, 1990, p. 21.

[30] R. Marqués, M. J. Freire, and J. D. Baena, "Theory of three-dimensional subdiffraction imaging," *Appl. Phys. Lett.*, vol. 89, p. 211113, Nov. 2006.

Alex M. H. Wong received the B.A.Sc. degree in engineering science and the M.A.Sc. degree in electrical engineering from the University of Toronto, Toronto, ON, Canada, in 2006 and 2009, respectively, where he is working toward the Ph.D. degree.

His research interests include high resolution imaging using electromagnetic waves, sub-wavelength focusing devices, metascreens and superoscillations.

George V. Eleftheriades (F'06) received the Diploma in electrical engineering from the National Technical University of Athens, Greece, in 1988, and the M.S.E.E. and Ph.D. degrees in electrical engineering from the University of Michigan, Ann Arbor, in 1989 and 1993, respectively.

From 1994 to 1997, he was with the Swiss Federal Institute of Technology, Lausanne. Currently, he is a Professor in the Department of Electrical and Computer Engineering, University of Toronto, ON, Canada, where he holds the Canada Research Chair/Velma M. Rogers Graham Chair in Engineering.

Prof. Eleftheriades was elected a Fellow of the Royal Society of Canada, in 2009. He was the recipient of the 2008 IEEE Kiyo Tomiyasu Technical Field Award, the 2001 Ontario Premiers' Research Excellence Award, and the 2001 Gordon Slemon Award presented by the University of Toronto, and the 2004 E.W.R. Steacie Fellowship presented by the Natural Sciences and Engineering Research Council of Canada. He is the co-recipient of the inaugural 2009 IEEE Microwave and Wireless Components Letters Best Paper Award. One of the papers he coauthored received the RWP King Best Paper Award in 2008. He has served as an IEEE Antennas and Propagation-Society (AP-S) Distinguished Lecturer (2004–2009) and as a member of the IEEE APS Administrative Committee (AdCom, 2008–2010). He is an Associate Editor of the IEEE TRANSACTIONS ON ANTENNAS AND PROPAGATION and a member of Technical Coordination Committee MTT-15 (Microwave Field Theory). He has been the General Chair of the 2010 IEEE Int. Symposium on Antennas and Propagation and CNC/USNC/URSI Radio Science Meeting held in Toronto.